Performance improvement of deorbitalized exchange-correlation functionals

H. Francisco [*]
Quantum Theory Project, Department of Physics, University of Florida, Gainesville, Florida 32611, USA

B. Thapa [†]
Department of Physics and Astronomy, George Mason University, Fairfax, Virginia 22030, USA

S. B. Trickey [‡]
Quantum Theory Project, Department of Physics and Department of Chemistry, University of Florida, Gainesville, Florida 32611, USA

A. C. Cancio
Department of Physics and Astronomy, Ball State University, Muncie, Indiana 47306, USA

(Received 12 September 2025; accepted 30 January 2026; published 3 April 2026)

Deorbitalization of a conventional meta-generalized-gradient exchange-correlation approximation replaces its dependence upon the Kohn-Sham (KS) kinetic energy density with a dependence on the density gradient and Laplacian. In principle, that simplification should provide improved computational performance relative to the original meta-generalized-gradient-approximation form because of the shift from an orbital-dependent generalized KS potential to a true KS local potential. Often that prospective gain is lost because of problematic roughness in the density caused by the density Laplacian and consequent roughness in the exchange-correlation potential from the resulting higher-order spatial derivatives of the density in it. We address the problem by constructing a deorbitalizer based on the "r^{2}SCAN piecewise polynomial" (RPP) deorbitalizer from A. D. Kaplan and J. P. Perdew [Phys. Rev. Mater. **6**, 083803 (2022)] with comparative smoothness of the potential along with retention of constraint satisfaction as design goals. Applied to the r^{2}SCAN exchange-correlation functional presented by J. W. Furness *et al.* [J. Phys. Chem. Lett. **11**, 8208 (2020)], we find substantial timing improvements for solid-state calculations over both r^{2}SCAN and its earlier deorbitalization for high-precision calculations of structural properties, while improving upon the accuracy of RPP deorbitalization for both solids and molecules.

DOI: 10.1103/rbf1-cp89

I. INTRODUCTION

The enormous impact of Hohenberg-Kohn-Sham density functional theory (DFT) upon computational study of molecular and materials properties is a consequence of the remarkable cost-accuracy balance of DFT when implemented with modern approximate exchange-correlation (XC) functionals. The cost-accuracy tradeoff is determined by the intrinsic limits and transferability of the specific XC approximation used. That compromise clearly differs by problem class. A small set of very large molecules can be treated with an XC approximation far up the Perdew-Schmidt "Jacob's ladder" complexity hierarchy [1]. In contrast, the computational costs of high-throughput screening calculations on large datasets of such molecules or *ab initio* molecular dynamics (AIMD) on counterpart condensed phases compel the use of lower-rung approximations. See, for example, the discussion in Secs. 2.2.21–23 of Ref. [2].

The SCAN meta-generalized-gradient approximation (meta-GGA) [3,4] and its variants [5–7] have proven to be effective compromises for accuracy and efficiency in structural and energetic calculations for both solids and molecules [4,8], albeit with some limitations [9,10]. A design advantage of such meta-GGA functionals is the introduction of inherently nonlocal density information through the use of the noninteracting [Kohn-Sham (KS)] kinetic energy density [11,12],

$$\tau_S := \frac{1}{2}\sum_i f_i |\nabla \phi_i(\mathbf{r})|^2 \tag{1}$$

with orbitals ϕ_i and occupation numbers f_i. [Throughout we consider only nonrelativistic and non-spin-polarized ($f_i = 0, 1, 2$) systems and use Hartree atomic units unless otherwise noted]. A resultant design advantage is satisfaction of many more exact constraints than possible with a GGA, particularly for the iso-orbital limit.

Despite the successes, there are difficulties of implementation with these meta-GGAs that limit their full exploitation. The explicit orbital dependence introduced by τ_S causes typical practical application to rely on nonlocal XC potentials in generalized KS (gKS) equations. Solutions to those

[*]Contact author: francisco.hector@ufl.edu
[†]Contact author: bthapa3@gmu.edu
[‡]Contact author: trickey@ufl.edu

can be slow relative to pure KS implementations [13]. This slowness also originates with the complicated form of the functionals and their potentials, their consequent sensitivity to the density [14], and the concomitant need for dense grids for converged integrals [15,16]. Calculations are sometimes done non-self-consistently [8,17]. Projector-augmented wave (PAW) effective potentials for these functionals have proven difficult to develop [14].

Effort to resolve these issues has led to the redesign of SCAN, first by streamlining performance at the cost of significant constraint noncompliance [6], then by iso-orbital indicator redefinition [5], and, most recently, in r^{2}SCAN [7], by restoration of most of the constraints met by SCAN, while retaining the improvements in numerical performance of prior variants. Nonetheless, some numerical problems remain [14,16].

Deorbitalization [13,18,19] has been developed as a strategy both to obviate numerical issues stemming from use of gKS and to retain the interpretive power of the pure KS equation. In deorbitalization, the τ_S dependence used in meta-GGA XC functionals as a local indicator of bond character is replaced with a function of the density $n(\mathbf{r})$, its gradient ∇n, and Laplacian $\nabla^2 n$. The result is a pure XC density functional and a pure (local) KS potential.

The obvious deorbitalization requirement is a sufficiently accurate approximate orbital-free kinetic energy density (KED) functional, which is an active area of research [20]. A usefully accurate description of the KED for deorbitalizing a meta-GGA indicator functional by a simple GGA alone does not seem possible [13]. Inclusion of the density Laplacian proves essential for accurate orbital-free description of the KED at a local level, as demonstrated with the KED density functional provided by Perdew and Constantin [21] (and also Ref. [22]). Practical deorbitalization has come through the methodology of Mejía-Rodríguez and Trickey [13,18,19] (M-RT). They reparametrized existing Laplacian-level KED functionals, e.g., Perdew-Constantin (PC) [21] and others from orbital-free DFT [20], to match KED-dependent indicator functions of the first 18 isolated atoms. The most generally successful case of M-RT deorbitalization involves the reparametrization (PC$_{\rm opt}$) of original PC. That gave successful deorbitalizations of both SCAN [13,18] and r^{2}SCAN [19], in the sense of providing what was deemed to be a faithful reproduction of the parent meta-GGA error patterns for structural and energetic properties evaluated on standard molecular and crystalline benchmarks. Such faithfulness in reproduction defines a deorbitalization goal, one which we follow.

That faithfulness also has held up in application to materials and outside the original test sets [23,24]. Other KEDs, e.g., Cancio-Redd (CR) [25], have led, for some meta-GGAs [26], to better error patterns than those produced with the exact KED, but that has not been seen for best-in-breed meta-GGAs.

A limitation of the M-RT error-pattern criterion of deorbitalization faithfulness is that it can allow acceptance of deorbitalized XC functionals that deviate noticeably from the exact form in the limit of slowly varying density, i.e., constraint violation. In the context of rethinking the PC functional form, the recent OFR2 study [27] emphasized constraint satisfaction, including restoration of correct slowly varying limit behavior, which recovers fourth-order gradient expansion compliance lost in going from SCAN to r^{2}SCAN [6]. The resulting deorbitalization does well in calculations for solids (retaining the numerical advantages of rSCAN) but not as well as r^{2}SCAN-L (r^{2}SCAN deorbitalized by PC$_{\rm opt}$, the reparametrized version of PC used by M-RT [13,18]) for molecules.

As an aside for clarity, note that a second modification of the original M-RT deorbitalization has been developed [28] to treat meta-GGAs that rely on more than one iso-orbital indicator, particularly the Tao-Mo functional (TM) [29], which is not relevant here.

Alternative strategies to Laplacian-level deorbitalization include use of higher-order spatial derivatives [30–32] and deorbitalization of the exchange potential only [17]. Those are of only contextual interest here, as they may have more significant numerical challenges than those arising from the M-RT procedure.

Given the success at reproducing the test-case performance of existing orbital-dependent meta-GGAs, the challenge is the effective numerical implementation of such a deorbitalized functional. The well-known sensitivity to density Laplacians serves as a caution (see, e.g., the discussion in Ref. [13]). Laplacian-based XC deorbitalizers, like Laplacian-based KEDFs, can be ill-behaved with regard to integral convergence and require relatively dense grids [16]. Moreover, they also can have large, spiky variations in the magnitude of the XC potential. Such variations arise from the high-order spatial derivatives in the X potential that follow from $\nabla^2 n$ [27].

Nonetheless, some of the M-RT functionals [13,18] have shown marked performance improvement over their gKS parents, with time per self-consistent-field (SCF) cycle of the Kohn-Sham solution as much as a factor of 3 shorter with the VASP code [33,34]. But recent work indicates [28] that it is quite typical for deorbitalized functionals to require many more self-consistent cycles to achieve SCF convergence than for their parent functionals with gKS, thus offsetting the gains made per cycle.

The natural, critical question raised by these issues is this: Can deorbitalization, in fact, succeed in achieving faster, more reliable meta-GGA calculations? At a more detailed level, how does the difficulty of using $\nabla^2 n$ compare with the difficulties of gKS calculations? For which run conditions, and for which applications, if any, does deorbitalization provide a clear advantage? With respect to computational efficiency, where and how can M-RT deorbitalization be improved?

One clear opportunity is to find ways to reduce numerical instabilities induced by the density-Laplacian. In this work, we take a specific step in that amelioration by intervening in those aspects of the deorbitalized functional that are most problematic, while retaining (or even eventually restoring) important constraints along the way. Our scheme is based on exploitation of the Cancio-Redd [25] and Cancio-Stuart-Kuna [22] approach of minimizing the structural complexity of KED functionals. We combine that with the constraint satisfaction of the "r^{2}SCAN piecewise polynomial" (RPP) deorbitalized indicator function [27] used in the OFR2

functional to produce a deorbitalizer with a smoother X potential than OFR2. We show that this functional performs well compared to r^{2}SCAN and r^{2}SCAN-L (PC_{opt}) and as well or better than OFR2 for solid test cases. It improves significantly on OFR2 for molecular test sets but still is not as good for those as r^{2}SCAN-L (PC_{opt}). We leave until later a more systematic approach to constructing smoothed functionals along with a measure to assess the result.

Secondly, we report a study of timing characteristics, using a single compute node. We show that deorbitalization can be an attractive option for meta-GGA calculations, reproducing similar if not better results than original meta-GGA for solids and for equation of state calculations, being up to twice as fast in total compute time as gKS calculations. At the same time, we find a number of situations in which the two approaches are about equal in performance and slow compared to GGAs, indicating the need for future work.

In the remaining presentation, Sec. II details the deorbitalization approach and the various KED models utilized. Section III describes the methods for performing structural and timing benchmarks. Section IV reports the structural benchmarking and detailed timing analysis for solids, including preliminary *ab initio* molecular dynamics (AIMD) outcomes. Section V presents our conclusions and prospects for future work.

II. BACKGROUND

A. Meta-GGA structure

A conventional meta-GGA XC functional (ignoring spin-decomposition) is defined by

$$E_{\rm XC}[n] := \int d\mathbf{r}\, e_{\rm XC}[n(\mathbf{r}), \nabla n(\mathbf{r}), \tau_{\rm S}(\mathbf{r})], \tag{2}$$

where both the density n and noninteracting kinetic energy density $\tau_{\rm S}$ are expressed in terms of orbitals ϕ_i and occupation numbers f_i, with

$$n(\mathbf{r}) := \sum_i f_i |\phi_i(\mathbf{r})|^2 \tag{3}$$

and $\tau_{\rm S}$ given by Eq. (1). To cope with the explicit orbital dependence in the XC energy (and, therefore, implicit density dependence), customarily the ground-state energy is found via the gKS procedure. In it, the XC potential is calculated as the functional derivative of the energy with respect to the individual orbitals. The result is the gKS equation in which the kinetic energy operator becomes

$$-\frac{1}{2}\nabla^2 + \nabla\cdot\left(\frac{\partial e_{\rm XC}}{\partial \tau_{\rm S}}\right)\nabla, \tag{4}$$

thus including a dependence upon the XC energy beyond that of the multiplicative potential of the pure KS formulation. (In practical implementation, that term can be rendered as an orbital-dependent potential, hence still requiring a generalization of the KS procedure.)

In SCAN and descendants such as r^{2}SCAN, $\tau_{\rm S}$ enters the XC functional via the iso-orbital indicator α,

$$\alpha(n, \nabla n, \tau_{\rm S}) := \frac{\tau_{\rm S} - \tau_{\rm W}}{\tau_{\rm TF}}. \tag{5}$$

Here $\tau_{\rm W}$ is the von Weizsäcker KED, namely that of a system with a single occupied orbital and density n,

$$\tau_{\rm W} = \frac{1}{8}\frac{|\nabla n|^2}{n} \tag{6}$$

and $\tau_{\rm TF}$ is the KED of the homogeneous electron gas of density n,

$$\tau_{\rm TF} = \tfrac{3}{10}(3\pi^2)^{2/3} n^{5/3}. \tag{7}$$

Akin with other refinements of SCAN, r^{2}SCAN uses a regularized version of α,

$$\bar{\alpha} := \frac{\tau_{\rm S} - \tau_{\rm W}}{\tau_{\rm TF} + 0.001\tau_{\rm W}}. \tag{8}$$

This regularization is primarily to handle undesirable behavior for exponentially small densities. Nevertheless, α serves as a convenient point of reference from which to define orbital-free KE density models.

The central roles of α and $\bar{\alpha}$ make it helpful to summarize, for context, the key structural elements of r^{2}SCAN exchange. Following Eq. (2) with $e_{\rm XC} = n(\mathbf{r})(\epsilon_{\rm X} + \epsilon_{\rm C})$, for exchange we have

$$\epsilon_{\rm X}^{\rm r^2SCAN}(p, \bar{\alpha}) = \epsilon_{\rm X}^{\rm LDA}[n] F_{\rm X}^{\rm r^2SCAN}(p, \bar{\alpha}), \tag{9}$$

$$\epsilon_{\rm X}^{\rm LDA}[n] = -(3/4)(3/\pi)^{1/3} n^{1/3}, \tag{10}$$

$$F_{\rm X}^{\rm r^2SCAN}(p, \bar{\alpha}) = \left\{h_{\rm X}^1(p) + f_{\rm X}(\bar{\alpha})\left[h_{\rm X}^0 - h_{\rm X}^1(p)\right]\right\} g_{\rm X}(p). \tag{11}$$

Here, the dimensionless reduced gradient (squared) is

$$p := s^2 \equiv \frac{|\nabla n|^2}{4(3\pi^2)^{2/3} n^{8/3}}. \tag{12}$$

The $h_{\rm X}^1(p)$ is a GGA form that is a rather complicated function of p. It enforces the gradient expansion of exchange through second order for $\alpha \approx 1$. Switching between GGA forms for $\alpha \approx 1$ and the iso-orbital limit ($\alpha \approx 0$), and extrapolation to $\alpha \to \infty$, is accomplished with the function $f_{\rm X}(\bar{\alpha})$. It has two exponential regions ($\bar{\alpha} < 0$ and $\bar{\alpha} > 2.5$) joined by a seventh-order polynomial in $\bar{\alpha}$. $g_{\rm X}(p)$ is a damping function that goes to unity in the limit $p \to 0$ and goes to zero as p grows arbitrarily large. Detailed expressions are in the Supplemental Material for Ref. [7].

An important bound, given the centrality of α, is

$$\tau_{\rm S} \geqslant \tau_{\rm W} \;\Rightarrow\; \alpha \geqslant 0. \tag{13}$$

This may be recognized as the non-negativity of the contribution to the Kohn-Sham kinetic energy derived from Pauli exclusion. Note that the r^{2}SCAN switching function $f_x(\bar{\alpha})$ just described is set up to enforce this requirement even if numerical precision errors otherwise would violate it.

The indicator α is related trivially to the Pauli kinetic energy density, which is the subject of much of orbital-free DFT (OF-DFT) [20],

$$\tau_\theta := \tau_S - \tau_W \tag{14}$$

or

$$\alpha = \tau_\theta/\tau_{TF} \equiv F_\theta. \tag{15}$$

Here F_θ is the Pauli enhancement factor of OF-DFT.

To deorbitalize a conventional meta-GGA according to M-RT, the exact KS KED is replaced by an approximate orbital-free semilocal density functional

$$\tau_{OF} = \tau(n, \nabla n, \nabla^2 n). \tag{16}$$

The deorbitalized meta-GGA then is

$$E_{XC}[n] = \int e_{XC}\{n(\mathbf{r}), \nabla n(\mathbf{r}), \tau_{OF}[n(\mathbf{r}), \nabla n(\mathbf{r}), \nabla^2 n(\mathbf{r})]\} d\mathbf{r}. \tag{17}$$

Minimization of the total energy with respect to n then yields a pure KS equation with a local XC potential of the form

$$v_{XC} = \frac{\partial e_{XC}}{\partial n} + \frac{\partial e_{XC}}{\partial \tau_{OF}}\frac{\partial \tau_{OF}}{\partial n} - \nabla\cdot\left(\frac{\partial e_{XC}}{\nabla n} + \frac{\partial e_{XC}}{\partial \tau_{OF}}\frac{\partial \tau_{OF}}{\partial \nabla n}\right) + \nabla^2\left(\frac{\partial e_{XC}}{\partial \tau_{OF}}\frac{\partial \tau_{OF}}{\partial \nabla^2 n}\right). \tag{18}$$

In it, the first and third terms treat the explicit dependence of e_{XC} on n and ∇n, respectively, while the others treat implicit dependence through τ_{OF}. A closely related quantity is the OF kinetic energy potential

$$v_S := \left(\frac{\partial \tau_{OF}}{\partial n}\right) - \nabla\cdot\left(\frac{\partial \tau_{OF}}{\partial \nabla n}\right) + \nabla^2\left(\frac{\partial \tau_{OF}}{\partial \nabla^2 n}\right). \tag{19}$$

In the OF-DFT literature this is more commonly expressed as taking the functional derivative of a model Pauli KED, τ_θ, which yields the Pauli potential via

$$v_\theta = v_S - v_W, \tag{20}$$

with v_W the KE potential for τ_W.

Comparison of Eqs. (4) and (18) illuminates the distinct, key challenges for ordinary versus deorbitalized meta-GGA XC numerical implementations. A conventional, orbital-dependent meta-GGA introduces a complicated kinetic energy operator in addition to the ordinary local Kohn-Sham potential. A deorbitalized counterpart produces a purely local potential whose construction involves up to fourth spatial derivatives of the density, with concomitant possible numerical difficulties.

B. Deorbitalization models

An orbital-free KED functional of the general form Eq. (16) obviously can be decomposed as in Eq. (14). The result may be reduced by scaling constraints to

$$\tau_{OF}(n, \nabla n, \nabla^2 n) = F_\theta^{OF}(p, q)\tau_{TF}(n) + \tau_W(n, p). \tag{21}$$

Here F_θ is as in Eq. (15) and

$$q := \frac{\nabla^2 n}{4(3\pi^2)^{2/3} n^{5/3}} \tag{22}$$

is the dimensionless reduced density Laplacian, partner to the reduced density gradient p defined in Eq. (12). Other important constraints include α non-negativity [Eq. (13)] and the gradient expansion of F_θ for slowly varying density [35,36].

KED functionals that have proven particularly useful for deorbitalization share several characteristics. They are proper meta-GGAs, in that they depend upon n, p, and q. The design of most has followed, to some degree at least, the strategy employed in the PC KED functional [21], which is to build a model for the KED in the slowly varying density limit. Then, because models based on the formally correct gradient expansion in that limit vary much more slowly with p than the iso-orbital limiting case (the von-Weizsäcker functional, τ_W), eventually such models fail the non-negativity constraint [37], $\tau_S \geqslant \tau_W$. That failure is taken to indicate the onset of an iso-orbital or nearly iso-orbital spatial region, and the slowly varying KED is replaced by τ_W by means of a suitable switching function.

For PC and PC_{opt} (the reparametrized PC used by M-RT [13,18]), the KED for the slowly varying limit is a modified fourth-order gradient expansion for which the Pauli enhancement function is

$$F_{PC}^{SV} = \frac{1 + \Delta F_\theta^{(2)} + \Delta F_\theta^{(4)}}{\sqrt{1 + \left[\Delta F_\theta^{(4)}/(1 + 5p/3)\right]^2}}. \tag{23}$$

The superscript "SV" denotes "slowly varying." The ingredient quantities are the second- and fourth-order gradient expansion corrections

$$\Delta F_\theta^{(2)} := -\frac{40}{27}p + \frac{20}{9}q, \tag{24}$$

$$\Delta F_\theta^{(4)} := \frac{8}{81}q^2 - \frac{1}{9}pq + \frac{8}{243}p^2. \tag{25}$$

The second-order gradient correction $\Delta F_\theta^{(2)}$ consists of a $5p/27$ contribution from the kinetic energy gradient expansion minus a $5p/3$ factor from the von Weizsäcker KED [$\tau_W = (5p/3)\tau_{TF}$], which yields an overall negative slope with respect to p. Together with the possibility of negative q, this leads to eventual incipient violation of KED non-negativity, which forces the switch from slowly varying to the iso-orbital model form.

For PC, the interpolation function between the slowly varying form of the Pauli enhancement factor and the von Weizsäcker lower bound $F_\theta^W = 0$ takes the form

$$\Theta_{PC}(x) = \begin{cases} 0, & x \leqslant 0, \\ f_{PC}(x/x_0), & 0 < x < x_0, \\ 1, & x \geqslant x_0, \end{cases} \tag{26}$$

where

$$f_{PC}(t) = \left[\frac{1 + e^{1/(1-t)}}{e^{1/t} + e^{1/(1-t)}}\right]^b, \quad 0 < t < 1. \tag{27}$$

Putting things together, the final form is

$$\alpha_{PC} = F_\theta^{PC} = F_{PC}^{SV}\,\Theta_{PC}\left(F_{PC}^{SV}\right), \tag{28}$$

with the reminder that α and the Pauli enhancement factor F_θ are identical [Eq. (15)]. The original PC parameter values

are $x_0 = 0.5389$, $b = 3$. The $\mathrm{PC_{opt}}$ values are $x_0 = 1.784\,720$, $b = 0.258\,304$ [13], determined by fitting to the KED α values of small-Z atoms. That reparametrization helps to produce faithful deorbitalization of some meta-GGAs but comes at the cost of a somewhat inaccurate form for the slowly varying limit ($p, q \to 0$).

Some drawbacks of the PC model were uncovered in Ref. [22], which provided a modified form to fix them. The switching model Θ_{PC} was found to cause unphysical features in the KED in covalent bonds, particularly for systems treated with pseudopotentials. Concurrently, the PC limit for $q \to \infty$ and p finite causes an unphysical treatment of the exponentially decaying density in the asymptotic region of a molecule, characterized by $q \to \infty$ and $p/q \to 1$. The first problem can be resolved by use of a switching factor that obeys $\tau > \tau_{\mathrm{GE}}$ and is as smooth as feasible. The second problem can be resolved by recognizing that the second-order gradient expansion for the KED has the scaling behavior of the exact KED for an exponentially decaying density and also is valid for small p and q. Thus it can suffice as a bare-bones model for the slowly varying limit.

Those choices, with further refinement [25], lead to the CR model, namely

$$\alpha_{\mathrm{CR}} = 1 + \Delta F_\theta^{(2)} \Theta_{\mathrm{CR}}\left(\Delta F_\theta^{(2)}\right) \tag{29}$$

with

$$\Theta_{\mathrm{CR}}(z) = \left[1 - \exp\left(-\frac{1}{|z|}^{a}\right)[1 - H(z)]\right]^{1/a}. \tag{30}$$

$H(z)$ is the Heaviside unit step function. The exponent $a = 4.0$ produces reasonably close estimates for the total KE of atoms [25], while $a = 2.0$ produces somewhat smaller Pauli potentials.

The RPP deorbitalizer [27] is a PC variant designed specifically for deorbitalizing r^{2}SCAN while retaining constraint satisfaction. As such, it starts with the same form as Eq. (28),

$$\alpha_{\mathrm{RPP}} = F_{\mathrm{RPP}}^{\mathrm{SV}} \Theta_{\mathrm{RPP}}\left(F_{\mathrm{RPP}}^{\mathrm{SV}}\right), \tag{31}$$

where $F_{\mathrm{RPP}}^{\mathrm{SV}}$ is, as before, a meta-GGA suitable for the slowly varying limit, to wit,

$$F_{\mathrm{RPP}}^{\mathrm{SV}} = 1 + \Delta F_\theta^{(2)} + \Delta F_\theta^{\prime(4)} + \Delta F_\theta^{\mathrm{asy}}. \tag{32}$$

In this expression, the fourth-order term $\Delta F_{\theta'}^{(4)}$ has the form of Eq. (25) but with dramatically altered coefficients: $b_{qq} = 1.801\,019$, $b_{pq} = -1.850\,497$, and $b_{pp} = 0.974\,002$. Those correct a corresponding error in the r^{2}SCAN exchange functional to restore gradient expansion compliance to fourth order in the slowly varying limit. The last term of Eq. (32) is higher than fourth-order and defines the asymptotic large p, q behavior. It is given by

$$\Delta F_\theta^{\mathrm{asy}} = c_3 p^2 (e^{-|c_3|p} - 1) + \left(\Delta F_\theta^{\prime(4)} - c_3 p^2\right) \times \left\{\exp\left[-\left(\frac{p}{c_1}\right)^2 - \left(\frac{q}{c_2}\right)^2\right] - 1\right\}. \tag{33}$$

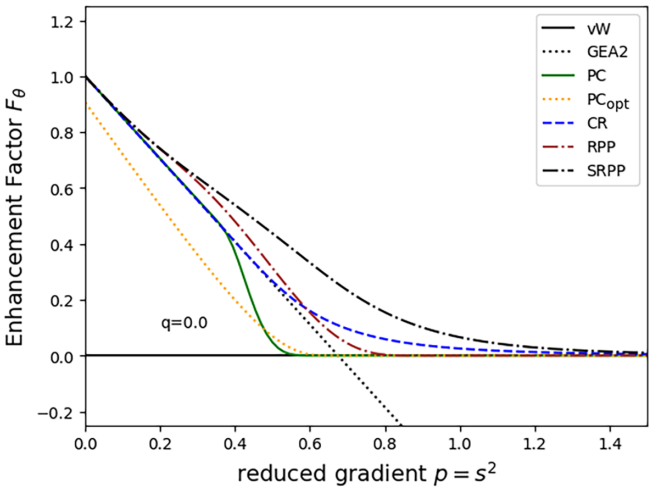

FIG. 1. Pauli enhancement factor $F_\theta(\equiv \alpha)$ for various KED functionals as a function of reduced density gradient p with reduced Laplacian $q = 0$. Models used are GEA ($= 1 + \Delta F_\theta^{(2)}$), PC [Eqs. (23)–(28)], $\mathrm{PC_{opt}}$ (same form, altered coefficients), CR [Eqs. (29) and (30)], RPP [Eqs. (31)–(37)], and SRPP [Eq. (38)]. $\alpha^{vW} = 0$ by construction.

This imposes the second-order gradient expansion as the limit for $p, q \to \infty$, p/q finite, as in CR. Optimal coefficient values were determined against appropriate norms [27] to be

$$c_1 = 0.202\,352, \tag{34}$$

$$c_2 = 0.185\,020, \tag{35}$$

$$c_3 = 1.538\,04. \tag{36}$$

The switching functional Θ_{RPP} involves the same piecewise logic as in PC, Eq. (26), but with the nonanalytic switching function f_{PC}, Eq. (27), replaced by the polynomial

$$f_{\mathrm{RPP}}(t) = 20t^3 - 45t^4 + 36t^5 - 10t^6. \tag{37}$$

The switching constant $x_0 = 0.819\,411$. (There is no b constant to set.)

In our context, a rather obvious step is to seek a smoothed RPP (SRPP) functional by replacing the RPP switching functional with the CR form,

$$\alpha_{\mathrm{SRPP}} = 1 + \left(F_{\mathrm{RPP}}^{\mathrm{SV}} - 1\right)\Theta_{\mathrm{CR}}\left(F_{\mathrm{RPP}}^{\mathrm{SV}} - 1\right). \tag{38}$$

A somewhat smoother functional, denoted SRPP2, arises from employing the exponent $a = 2$ in Θ_{CR}.

Figure 1 shows how these design choices affect the behavior of the Pauli enhancement factors, i.e., the α to be used in deorbitalization. That figure presents F_θ versus p for the specific value $q = 0$. The von-Weizsäcker lower bound value of $F_\theta^{\mathrm{W}} = 0$ appears as a black solid line. GEA2 denotes the gradient expansion model $1 + \Delta F_\theta^{(2)}$ that characterizes the slowly varying limit, $p, q \to 0$. The slowly varying limit for the PC meta-GGA starts at the homogeneous electron gas value of 1 at $p = 0$ and at first follows along the GEA2 trajectory. But GEA2 transgresses the von Weizsäcker bound before $p = 0.8$. (Recall the negative slope in the p-coefficient of the gradient expansion discussed earlier.) The switching function

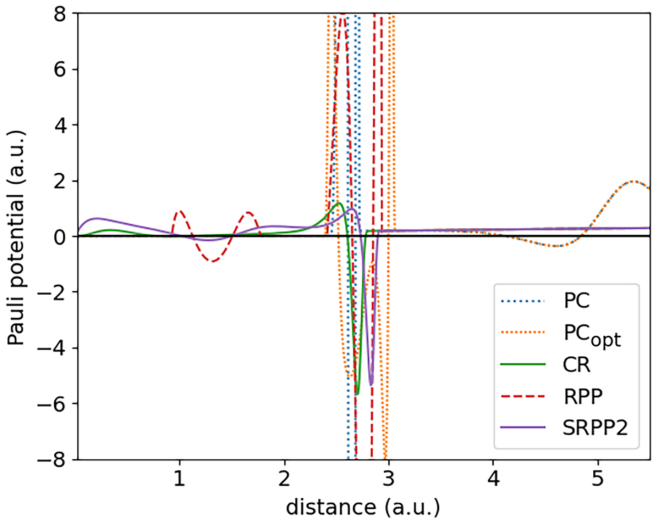

FIG. 2. Pauli kinetic potential $v_\theta = v_\tau - v_W$ for various Laplacian-level KED functionals for the hydrogen atom, evaluated at the exact atomic density. The exact value for the H atom, $v_\theta = 0$, is at the solid black line.

Θ_{PC} avoids that crossing by inducing the sudden dip in PC off the GEA2 onto the subsequent zero value, thus complying with the non-negativity constraint for F_θ. That dip is a fairly clear candidate to suspect as the cause of fluctuations in the PC Pauli potential and in the potential of a XC functional deorbitalized with PC. The dip leads to rapid variations in the PC KED in regions of near iso-orbital density, such as covalent bonds [22], which would be exacerbated in calculating the potential. This supposition is shown to be borne out in the following section. In contrast, the CR model (blue-dashed) and SRPP (black dot-dashed) make the transition (from GEA2 to von Weizsäcker bound) in a much smoother fashion, while RPP is an intermediate case. Finally F_θ for PC$_{opt}$ fails to satisfy the homogeneous electron gas limit ($F \to 1, p, q \to 0$) but does have a reasonably smooth transition.

C. Kinetic and exchange potentials

The smoothing problems that arise in the deorbitalizers are well-illustrated by a plot of the kinetic potential $v_\theta = \delta T_\theta / \delta n$, Eq. (20), for various relevant Laplacian-dependent KED functionals for the Hydrogen atom, evaluated with the exact H atom density. See Fig. 2. Most of the approximate KED functionals deliver potentials that are reasonably close to the exact value (zero) except in the vicinity of 2.5–3.0 a.u. There violent fluctuations in the potential are evident. Those can be traced to a spurious diagnosis of density behavior. At high densities, the KED functionals diagnose hydrogen to be an iso-orbital system, which is correct. But at low density they treat it like a slowly varying electron gas. The fluctuations occur for the values of r where the transition between the two behaviors occurs. The problem is worst for PC which suffers oscillations larger than 100 hartrees. The problematic behavior is somewhat less severe for PC$_{opt}$ and RPP with oscillations in the tens of hartrees. Only the CR model [25] and its extension to the RPP form, SRPP2, show more reasonable variations, on the order of a few hartrees. In fact, the size of those variations is correlated closely (with the exception of PC$_{opt}$) with the abruptness of the function used to describe the transition (from iso-orbital to slowly varying electron gas) in the enhancement factor, as seen in Fig. 1. As a caution, we note that the plot shows potentials evaluated with the exact ground-state density for hydrogen. The unreasonable oscillatory behavior almost certainly would be worse for self-consistent densities from the associated potentials.

Figures 3 and 4 show plots of the local part of the exchange potential [Eq. (18)] for the parent meta-GGA functional (r^{2}SCAN) and the full X potential for three deorbitalized versions of it (PC$_{opt}$, RPP, and SRPP). The systems are the H atom (at two different length scales) and the Si atom. [Note that r^{2}SCAN deorbitalized with the RPP form has the formal functional name OFR2. As a generalizable name for any deorbitalized meta-GGA that is reasonably compatible with previous usage, e.g., M-RT, from here on we have adopted the portmanteau of meta-GGA, "-L" (for Laplacian dependence), and deorbitalizer name in parentheses. Our new deorbitalizations of r^{2}SCAN thus are r^{2}SCAN-L(SRPP) and (SRPP2). For simplicity in making comparisons between deorbitalization options, where context allows, frequently we will refer to the deorbitalizer name, not the full functional name.] Note that the X potential in Fig. 3 is multiplied by the radial coordinate to bring out features near the valence edge where most variation in potentials occurs. For r^{2}SCAN, the contribution from the functional derivative with respect to the kinetic energy density is omitted, as it is incorporated in the physics of the gKS scheme via Eq. (4). These potentials are computed using a modified version of the PYTHON code *densities* [38] which employs fixed analytic spherical densities obtained from self-consistent Hartree-Fock calculations [39] They were evaluated on a double-exponential grid with 1000 radial points, with substantially more points for r^{2}SCAN.

First, we note a comparison with a prior calculation of the r^{2}SCAN-L(RPP) (OFR2) X potential as a function of radial distance for the hydrogen atom, Fig. 7 of Ref. [27]. Even allowing for how the information is displayed [$rV_X(r)$ on the y axis here versus $V_X(r)$ in the other paper and r on a log scale here versus uniform in the other], it is clear that the two noise profiles are profoundly different. Ours shows considerably less noise, assuming any sharp feature in the potential outside the cusp region to be noise induced. As shown in the Supplemental Material [40], we have analyzed the dependence of the numerically calculated X potential upon grid density. We find oscillations of magnitude similar to those shown in Ref. [27] when our grid has 300 points. Those vanish with finer grids and converge to the value shown here for a grid size greater than 700 points. We also verify that the two potentials, when plotted in the same fashion, are essentially identical up to noise. We do not know if the prior work included a noise sensitivity analysis, but doing so seems to be an important consideration when working with the density Laplacian.

Though an unequivocal comparison of the gKS local part and ordinary KS potentials is not possible, it is clear that deorbitalization of r^{2}SCAN introduces unphysical oscillations. In particular, we see large noise in the region $r \approx 3$ au for the H atom, where the Pauli potential, Fig. 2, is seen to fail. However, the SRPP deorbitalization of r^{2}SCAN [r^{2}SCAN-

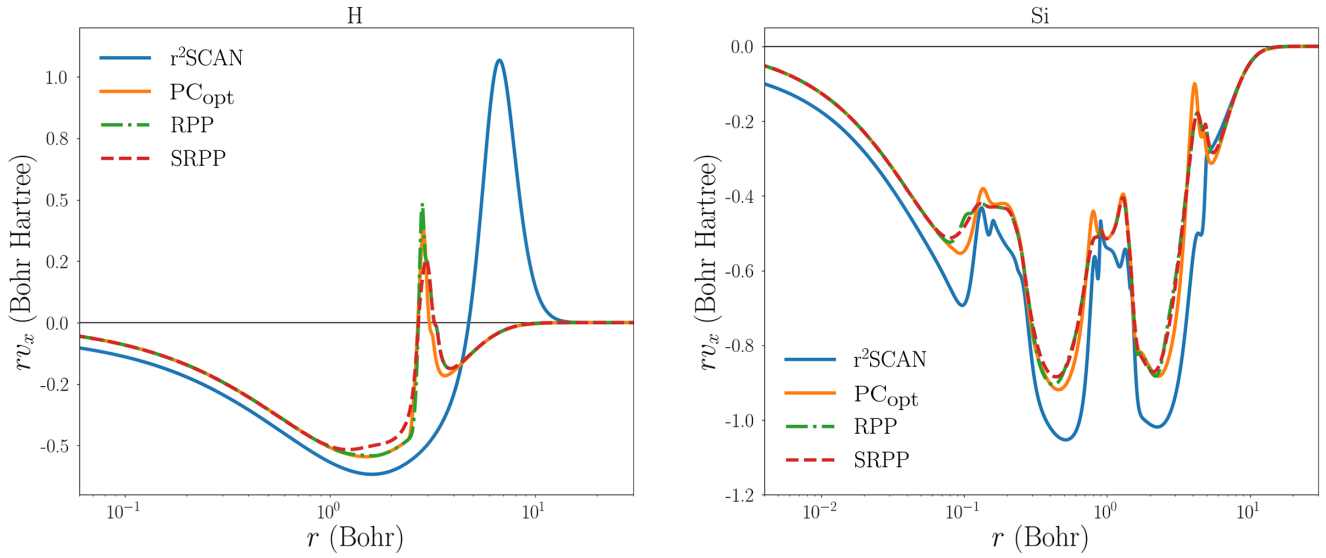

FIG. 3. Local part of the r^{2}SCAN exchange potential for the H and Si atoms (scaled by radius r) compared to the exchange potentials of several deorbitalized versions of r^{2}SCAN for the same atoms.

L(SRPP)] results in modestly less noise in the potential compared to the PC$_{\rm opt}$ or RPP deorbitalizations. A similar trend occurs for Si, with SRPP slightly smoother than RPP and both smoother than PC$_{\rm opt}$. Interestingly, the RPP and SRPP produce potentials noticeably smoother overall than the local part of the parent meta-GGA, despite use of the density Laplacian. (To be sure that this indeed is true, we needed to increase the resolution for the r^{2}SCAN results to 10 000 points for H and 40 000 for Si).

The noticeable bump in the r^{2}SCAN H atom potential at large r [Fig. 3(a)] may be a remnant of a major issue in the original SCAN. In a region of exponentially decaying density, v_x for SCAN goes to a large positive value rather than zero [6,7]. That unphysical behavior forces the use of extremely fine grids and leads to difficulties in obtaining pseudopotentials [14]. (Note that the exact KS exchange potential for the H atom must cancel the self-Hartree potential, hence rv_x must go asymptotically to -1, which no potential considered here does properly).

The short-range behavior for any atom is exemplified by the H atom case. All potentials for it fail by diverging at extremely small distances, rather than trending to a small negative value [41]. Overall v_x from PC$_{\rm opt}$ and SRPP are rather close. Unlike v_x from RPP, they are roughly similar quantitatively to the parent v_x.

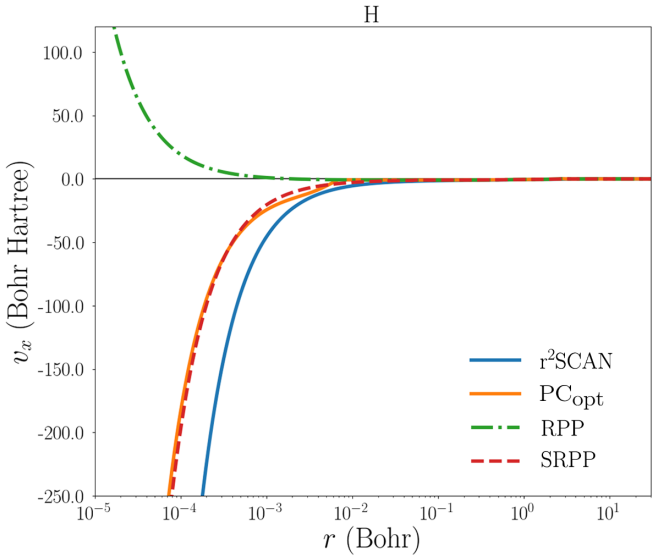

FIG. 4. The local part of the r^{2}SCAN X potential for atomic H compared to deorbitalized X potentials, plotted over a much larger range in length and energy.

D. Noise problem quantification

The unphysically noisy features in the Pauli kinetic potentials shown in Fig. 2 can be diagnosed readily as arising primarily from the density Laplacian term, i.e., the last term of Eq. (20). Clearly it is closely related to the last term in Eq. (18) for the exchange-correlation potential. This makes sense since both have the Laplacian of a functional of the Laplacian of the density. Thus fourth spatial derivatives of the density arise in both as well as third derivatives of $e_{\rm XC}$ in the latter case. Those high-order spatial derivatives intrinsically accentuate oscillations in a function. Reduction of the magnitude of this term should lead to smoother potentials. The reduction in v_θ oscillations from PC to CR shown in Fig. 2 is commensurate with that supposition. Such reduction should yield more efficient numerical performance.

For a quantitative assessment of the extent to which that supposition is correct, we borrow a measure from electrostatics. Observe that satisfaction of Laplace's equation

$$\nabla^2\psi = 0 \tag{39}$$

by some function ψ within a specified spatial region is the condition for minimizing the action defined by

$$I = \frac{1}{2}\int |\nabla\psi|^2 dV \tag{40}$$

TABLE I. Kinetic energy and integrated noise measure I^{deorb} evaluated on the hydrogen atom for several deorbitalized models of the KE density.

Model	Exact	PC	PC_{opt}	RPP	CR	SRPP	SRPP2
KE (ha)	1/2	0.507	0.506	0.504	0.514	0.527	0.550
I (a.u.)	0	220	44.0	19.0	1.705	1.755	1.555

with respect to variations in ψ, with the value of ψ on the boundary of the solution region fixed.

The impact of the Laplacian term in the kinetic potential thus can be measured by calculating the action for an appropriate ψ. Here we choose

$$I^{\text{deorb}} = \frac{1}{2}\int \left|\nabla\left(\frac{\partial\tau}{\partial\nabla^2 n}\right)\right|^2 dV. \tag{41}$$

This technique has been applied previously to minimize the Laplacian term of the overall exchange-correlation potential—see Ref. [42] for details. Our choice to concentrate on the kinetic potential reflects the fact that the Laplacian term of the X potential actually generates two plausibly problematic contributions. One, $\nabla^2(\partial e_{\text{XC}}/\partial\tau)$, arises from the functional dependence of e_{XC} on τ. The other, $\nabla^2(\partial\tau/\partial\nabla^2 n)$, arises from the dependence of the deorbitalization of τ on $\nabla^2 n$. The effects of the form of $e_{\text{XC}}(\tau)$ upon performance characteristics of both conventional and deorbitalized meta-GGAs has been the subject of recent attention [6,7,27]. However, comparison of Fig. 2 to Fig. 3 shows that the location of major error in the hydrogen X potential (the bump in deorbitalized potentials around 2 to 3 a.u.) coincides with that of dramatic noise in the Pauli potential. This implicates, strongly, the second term as a culprit in generating X potential noise, hence that term is a focus of concern. A second benefit of this choice is to focus on an aspect of the potential that is independent of the choice of XC functional being deorbitalized.

Minimization of oscillations in that term on a useful test density or densities would have the potential of minimizing its impact on numerical performance in general. Perhaps that should be a design goal for a deorbitalized functional. We will explore that idea in a follow-up to the present study. For now, to get an efficient, useful estimate of the impact of deorbitalizer-generated noise, we simply evaluate Eq. (41) for the H atom as calculated from a given KED functional. The crucial point is that the exact Pauli potential, Eq. (20), for this case is zero.

The consequences of that evaluation are shown, along with the kinetic energy obtained by integrating τ_{OF}, in Table I with the deorbitalizers PC, PC_{opt}, CR, RPP, SRPP, and SRPP2. There is a close correlation between the smoothness of transition between slowly varying and iso-orbital limits exhibited by the enhancement factors seen in Fig. 1 and the quantified measure I^{deorb}. The switching behavior of PC clearly is the most abrupt. Thus it has an enormous I^{deorb} value. PC_{opt} and RPP do much better, with a reduction in I^{deorb} by a factor of 5 and an order of magnitude respectively. Clearly, the functionals with the CR switch (CR, SRPP, SRPP2) are the best. That pattern is manifest to a considerable extent in the corresponding kinetic potentials (Fig. 2) and to a lesser but still significant extent for X potentials, Fig. 3.

The next issue, obviously, is to address to what extent (if any) this smoothing endeavor and its quantitative assessment has consequences for calculations on real systems.

III. COMPUTATIONAL METHODS

For molecular system tests, calculations were done with the NWCHEM 7.0.2 code [43] using the def2-TZVPP basis set and `xfine` grid settings. Test comparisons are to heats of formation computed according to the now-standard procedure of Curtiss *et al.* [44,45] for the 223 molecules of the G3X/99 test, to bond lengths for the T96-R test set [46,47], and to harmonic vibrational frequencies using the T82-F test set [46,47].

Solid structural properties were calculated with the VASP-5.4.4 code [34], following the same methodology and protocol as in Ref. [48].

In particular, we used projector augmented wave (PAW) methodology with PBE-based datasets, consistent with previous M-RT studies [18]. (Since PAWs for meta-GGAs are unavailable in VASP, use of PBE PAW datasets for meta-GGAS in VASP calculations is accepted practice.) For hexagonal close-packed structures the ideal c/a ratio was used. For cohesive energies, isolated atom energies were calculated using a $14 \times 15 \times 16$ Å unit cell and Γ-point sampling. Static-crystal lattice constants and cohesive energies are compared to published results for 55 solids [49] and, correspondingly, for bulk moduli of 44 solids [50]. In addition, band gaps of 21 insulators and semiconductors [51] were computed. Equilibrium lattice constants a_0 and bulk moduli B_0 at $T = 0$ K were determined by calculating the total energy per unit cell at 12 points in the volume range $V_0 \pm 10\%$, where V_0 is the calculated equilibrium unit cell volume, followed by fitting to the stabilized jellium equation of state (SJEOS) [52]. All the error values are from comparison with tabulated experimental values.

For timing calculations, the same methodology was used except that for the 55 solids [49] test set, the calculations were redone at the experimental lattice constants. In that way only single-point energy evaluations were needed for timings. Calculations used a single node on the University of Florida HiperGator system (Gen. 3) with an AMD EPYC 75F3 32-core processor with 4GB of memory per core. They were executed in parallel across all 32 cores.

IV. RESULTS

A. Atoms

An issue raised by moving from the RPP to SRPP is norm compliance. The free coefficients c_1, c_2, and c_3, are determined in the RPP by fitting to (i) the XC energy of noble gas atoms Ne, Ar, Kr, Xe; (ii) "cluster" energies of jellium clusters; and (iii) surface energies of jellium clusters. In developing the SRPP with the goal of smoothing the potential relative to RPP, we have not modified any aspect of the RPP except for the transition between the slowly varying and iso-orbital limits. The c coefficients and other parameters in the slowly varying form of RPP are left unchanged. Thus, it

TABLE II. Comparison of molecular structural property results for the r^{2}SCAN XC functional and various deorbitalized-(r^{2}SCAN-L) variants derived from PC$_{opt}$, RPP, SRPP, and SRPP2 KED functionals. PBE results included for context. Heat of formation mean errors (ME), mean absolute deviation (MADs), and spread in kcal/mol, bond length errors in Å, and frequency errors in cm^{-1}.

				r^{2}SCAN-L			
		PBE	r^{2}SCAN	PC$_{opt}$	RPP	SRPP	SRPP2
Heats of formation	ME	−20.878	−3.145	1.845	8.796	−5.918	−9.470
	MAD	21.385	4.488	5.300	13.109	7.804	10.405
	Spread	88.091	29.818	42.938	72.117	48.329	46.036
Bonds	ME	0.018	0.005	0.008	0.014	0.011	0.013
	MAD	0.018	0.010	0.011	0.014	0.012	0.014
	Spread	0.168	0.183	0.197	0.182	0.069	0.180
Frequencies	ME	−33.781	11.336	−7.248	−26.743	−22.875	−22.945
	MAD	43.613	30.899	25.709	36.711	36.134	36.800
	Spread	261.16	212.42	201.73	266.59	276.09	268.84

would be unsurprising if the norms fit by them were to be less well met in SRPP than in RPP.

We can test the effect that replacing the piecewise polynomial transition function [Eqs. (26) and (37)] in RPP with the smoother SRPP function [Eq. (30)] has on satisfaction of the "appropriate norm" of atomic exchange-correlation energies. We calculated self-consistent RPP and SRPP exchange-correlation energies for atoms up through $Z = 18$ using NWCHEM, with the same basis sets as for molecules. As benchmark energies, we take highly accurate correlation energies from Ref. [53] and exact exchange calculation values using the optimized effective potential code OPMKS [54].

Overall, we find a mean error of about 2.1% for the RPP and 2.8% for SRPP, both systematically negative. This error decreases gradually in magnitude with system size. That decrease is expected since the XC energy of large-Z atoms is increasingly well-characterized by the slowly varying electron gas as $Z \to \infty$ [55], and each functional matches that limit as a norm. The discrepancy between RPP and SRPP for atoms between $Z = 10$ and 18 is about 0.5%, decreasing rapidly with Z. This rapid decrease is consistent with the decrease in importance of the cusp region and the exponential decay of the density far from the nucleus, the two regions in which the transition from gradient expansion to von Weizsäcker behavior is most important. See the Supplemental Material [40] for more details.

We lack the capacity to test compliance with the jellium norms, but we expect similar results.

B. Structural properties

Evidently the comparison of primary interest is for r^{2}SCAN versus its deorbitalized versions, r^{2}SCAN-L(PC$_{opt}$), with the PC$_{opt}$ deorbitalizer [19], as well as with r^{2}SCAN-L(RPP) [27] and with r^{2}SCAN-L(SRPP) and (SRPP2). An underlying issue, discussed in detail above, is that PC$_{opt}$ breaks some constraints that the other three preserve. That distinction motivates further comparison, namely between PC$_{opt}$ and the three more constraint-compliant deorbitalizers.

Tables II and III compile mean errors (MEs) and mean absolute deviations (MADs) for r^{2}SCAN, and deorbitalized r^{2}SCAN, for the four deorbitalizers, along with results from PBE [56] as a baseline. In addition to those standard measures of functional performance, we include the spread of errors as defined by the maximum (most positive) error minus the minimum (most negative.) This last measure is motivated by the wide variations in timing performance that we discuss below. That variability raises the question whether there might be similar variability in predictive performance. For molecular systems, the results presented in Table II show that SRPP is a substantial improvement (40% reduction) over RPP for heat of formation MAD. SRPP2 also provides an improvement over RPP, albeit a significantly smaller one. On bond lengths and vibrational frequencies, the three (RPP, SRPP, SRPP2) perform about the same. None proves competitive with PC$_{opt}$. All three RPP-derived deorbitalizations show a disappointing degradation of performance, especially for heats of formation and frequencies, compared to PC$_{opt}$ deorbitalization, and none can be considered a completely faithful deorbitalization of r^{2}SCAN. Also note the near equality of the magnitude of MEs and MADs for SRPP2 and to a lesser extent, SRPP. This, and the fact that the MEs for both are negative, indicate that they tend to underbind consistently, leading to larger MADs.

For solids, Table III shows quite different outcomes. SRPP, SRPP2, and RPP all have distinctly better MADs than PC$_{opt}$ for lattice constants, cohesive energies, and bulk moduli. SRPP and SRPP2 are a tiny bit better than RPP on lattice constant MAD, slightly worse (3%) on cohesive energy, and about 9% better on bulk modulus. The bulk modulus spread for SRPP and SRPP2 is better than for RPP as well and substantially better than that from PCopt.

Overall, SRPP and SRPP2 preserve the formal properties of RPP and either improve on its performance or maintain it. RPP is already known to be better on metallic solids than PC$_{opt}$ (and better in some measures than r^{2}SCAN) but worse on molecules [27]. That behavior is confirmed by our results (again, see Tables II and III). Among the three, SRPP and SRPP2 are slightly better than RPP for solids, while SRPP is the best of the three over all systems though not competitive with PC$_{opt}$ for molecules. These outcomes reinforce the finding by Kaplan and Perdew [27] that reintroduction of compliance with constraints broken by PC$_{opt}$ actually can reduce the breadth of applicability of the deorbitalization.

TABLE III. As in Table II for solid-state structural properties. Mean errors (MEs), mean absolute deviations (MADs) and spreads for equilibrium lattice constants in Å, cohesive energies in eV/atom, bulk moduli in GPa, and band gaps in eV.

				r^{2}SCAN-L			
		PBE	r^{2}SCAN	PC_{opt}	RPP	SRPP	SRPP2
Lattice constants	ME	0.046	0.026	0.022	0.003	−0.003	−0.002
	MAD	0.053	0.037	0.038	0.029	0.028	0.028
	Spread	0.222	0.311	0.212	0.154	0.143	0.142
Cohesive energies	ME	−0.070	−0.134	−0.327	−0.017	0.051	0.064
	MAD	0.252	0.238	0.349	0.217	0.224	0.227
	Spread	2.096	2.343	1.841	1.726	1.773	1.801
Bulk modulus	ME	9.704	1.367	−4.249	1.084	1.928	2.228
	MAD	11.022	5.963	10.115	8.542	7.866	7.851
	Spread	64.09	63.67	96.90	81.64	76.25	76.25
Band Gaps	ME	−1.69	−1.20	−1.38	−1.60	−1.58	−1.57
	MAD	1.69	1.20	1.38	1.60	1.58	1.57
	Spread	4.89	4.32	4.72	4.99	4.93	4.92

The error spread reduction provided by the RPP-derived models was unexpected. Those spreads are quite a bit better than the original r^{2}SCAN for both cohesive energies and lattice constants and not much worse for bulk moduli. In that regard, PC_{opt} shows some degradation. Similar results are found if we measure standard deviations. That is to say, deorbitalization can, in some cases, lead to a significant reduction in outliers compared to the gKS calculations with the parent meta-GGA XC functional, an unexpected bonus. The inverse correlation of spread to our measure of potential smoothness is suggestive. If some of that spread is due to numerical instability rather than functional accuracy, these results would be a trade-off between removing numerical problems with gKS and introducing problems with the Laplacian. The relative absence of outliers leads us to speculate that the noise reduction in smoothed deorbitalized potentials may reduce the risk that geometry optimization procedures will discover spurious local minima.

C. Timing results

Table IV presents timing statistics for the 223 molecule G3X/99 test set. Table V displays the timing data for the six-molecule subset, denoted AE6, of the G3 test set. Each table shows the total time for the run of a test set, and the average time taken per system. In addition, each table shows the average number of SCF cycles needed to converge to self-consistency (defined as the total number of SCF cycles divided by the number of systems) and the average time per SCF cycle, taken as the average time divided by the average number of cycles. In Table IV, spreads in these last two measures are shown also. As before, spreads are defined as the difference between the maximum and minimum values of a quantity observed across a dataset.

Table IV shows that both r^{2}SCAN-L(SRPP) and (SRPP2) are substantially faster than r^{2}SCAN-L(RPP) for the molecules. Similar to the PC_{opt} deorbitalization, neither of them delivers a speed advantage over the parent, orbital-dependent functional. The effects of test-set sampling are shown in Table V. The AE6 timings give a much more favorable comparison of SRPP2 over RPP but no meaningful gain for SRPP2 versus either PC_{opt} or the parent r^{2}SCAN functional. Methodological effects are shown in Table VI. It gives the timings for the G3 test with the VASP 5.4.4 calculations done as isolated systems in a large orthorhombic box. Distinct from the solid calculations, the default cutoff energy was set to 600 eV and Γ point sampling was used. Unlike the G3 calculations in NWCHEM, the VASP tests exhibit a large degradation in performance by both RPP and SRPP deorbitalizations with respect to the parent functional. Interestingly, the time per SCF cycle for the SRPP deorbitalizer is 1.29 s/cycle

TABLE IV. Timings and number of SCF cycles required for computing the 223 molecules of the G3X/99 test set. Time measurements are expressed in seconds (s).

		r^{2}SCAN-L				
223 molecules	r^{2}SCAN	PC_{opt}	RPP	SRPP	SRPP2	PBE
Total time	2432.00	2410.90	3036.90	2433.60	2373.70	1417.70
Average time	10.91	10.81	13.62	10.91	10.64	6.36
Avg. number SCF cycles	7.79	8.07	8.42	8.19	8.28	8.45
Spread	23	24	24	24	24	22
Avg. time per SCF cycle	1.34	1.28	1.56	1.28	1.23	0.72
Spread	6.27	6.25	7.38	6.14	6.13	4.10

TABLE V. As in Table IV for the AE6 test set.

		r^{2}SCAN-L			
AE6	r^{2}SCAN	PC$_{opt}$	RPP	SRPP	SRPP2
Total time	25.40	25.40	35.00	27.20	26.00
Average time	4.23	4.23	5.83	4.53	4.33
Avg. number SCF cycles	6.50	6.33	8.33	7.17	7.17
Avg. time per SCF cycle	0.66	0.67	0.76	0.65	0.62

in VASP, while in NWCHEM it is 1.28 s/cycle. However, for the parent functional r^{2}SCAN, VASP takes 2.87 s/cycle compared to 1.34 s/cycle in NWCHEM. Unfortunately, the number of SCF cycles is much higher for the deorbitalized forms, roughly a factor of 2.5 for SRPP and a factor of 3 for RPP. In NWCHEM the average number of SCF cycles is roughly the same for all three. The speed advantage per cycle of the deorbitalized forms is lost thereby in the quasimolecular case. This brings to light the drastic effect that basis set methodology (plane-wave PAW versus Gaussian) can have on the performance of the deorbitalized forms.

For solids, Table VII presents a clearly different story. r^{2}SCAN deorbitalized with SRPP or SRPP2 outperforms the parent, orbital-dependent functional on total time. SRPP2 in particular needs only about 75% of the time of r^{2}SCAN. Notably, SRPP2 also requires only about 72% more time than PBE. This overall gain compared to the PC$_{opt}$ deorbitalization comes from a drastic reduction in the number of SCF cycles needed by SRPP and SRPP2, about half of the number required by PC$_{opt}$. Importantly, the times per SCF cycle for SRPP and SRPP2 are essentially the same as for RPP, less than half that for r^{2}SCAN, and actually faster than even for PBE. The combined result is an overall speedup.

The required number of cycles follows, reasonably closely, the measure of smoothness in the Laplacian contributions in the exchange potential (Table I), hence strongly implicates those terms in the slow SCF convergence performance seen in some of the deorbitalizations. We surmise that the sensitivity of such terms to rather small changes in the density makes achievement of a self-consistent density harder than in gKS or GGA calculations. This diagnosis is supported in the extreme spread of numbers of cycles for deorbitalized functionals compared to the parent functional as evaluated via gKS. The spread in observed cycle counts for r^{2}SCAN (gKS) is only slightly more than twice the average number of cycles, while for the deorbitalized forms (KS), the spreads range from 4.4 to 6.0, with SRPP2 the best performer.

TABLE VI. As in Table IV for the 223 molecules, but with the calculations done in VASP 5.4.4 for the functionals deorbitalized with RPP and SRPP as compared to the parent functional.

		r^{2}SCAN-L	
223 molecules	r^{2}SCAN	RPP	SRPP
Total time	11100.38	13573.66	13030.01
Average time	49.78	60.87	58.43
Average SCF cycles	17.22	51.90	43.14
Average time per SCF cycle	2.87	1.10	1.29

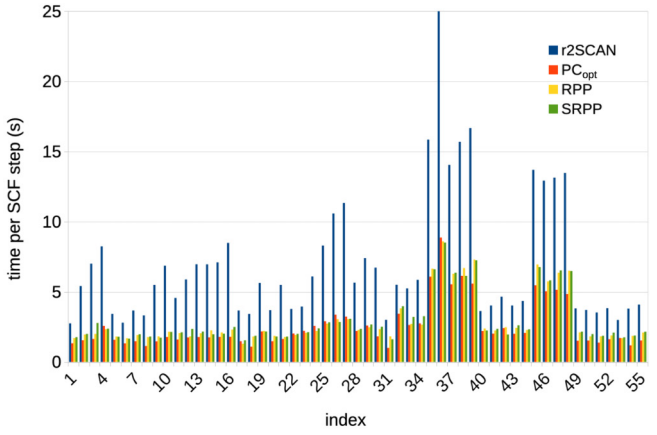

(a)

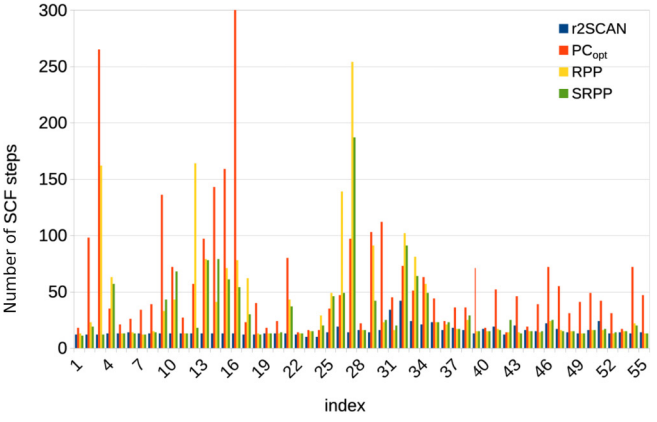

(b)

FIG. 5. Bar charts showing timing performance for r^{2}SCAN, and r^{2}SCAN-L with the PC$_{opt}$, RPP, and SRPP deorbitalizers for the entries in the 55-solid test set. Indexing of materials: 1–4 elemental semiconductors; 5–16: compound semiconductors; 17–22: ionic compounds; 23–31: simple metals; 32–55 transition metals. (a) Average time per SCF cycle in seconds, (b) Number of SCF cycles.

More insight can be found by visualizing the timings for the individual members of the solid test set. These are shown as average time per SCF cycle in Fig. 5(a) and number of SCF cycles in Fig. 5(b). Results for r^{2}SCAN itself as well as versions deorbitalized with PC$_{opt}$, with RPP, and with SRPP are shown. The distribution for SRPP2 is only modestly better than for SRPP, so it was omitted for clarity.

Figure 5(a) shows the clear SCF cycle-time advantage of the deorbitalized functionals versus their orbital-dependent parent, including the nearly three times faster performance of PC$_{opt}$ originally reported by M-RT. The other deorbitalizers are slightly less swift but still well above twice as fast as r^{2}SCAN per cycle. Notably, the issue is one of outliers. For about half the data set, the r^{2}SCAN (gKS) time is under 5 s and not quite two times slower than the deorbitalized forms (with KS potentials). But there are multiple bad actors in the orbital-dependent case. For them the slowdown is much worse. Deorbitalized functionals do poorly on a much smaller dataset of nine transition metals, all with nearly empty *d* shells, e.g., Y or Sc, or nearly empty spin subshells, like Fe.

TABLE VII. Timings and number of SCF cycles required for computing the 55 solids. Times are expressed in seconds (s).

		r^{2}SCAN-L				
55 solids	r^{2}SCAN	PC_{opt}	RPP	SRPP	SRPP2	PBE
Total time	6052.81	7812.30	6024.63	4892.41	4553.67	2650.44
Average time	110.05	142.04	109.54	88.95	82.79	48.19
Avg. number SCF cycles	15.64	60.31	40.35	30.49	31.42	14.20
Spread	32	341	242	176	138	19
Avg. time per SCF cycle	6.93	2.56	2.91	2.97	2.89	3.26
Spread	22.39	7.87	7.30	6.97	7.46	7.77

Figure 5(b) shows the number of SCF cycles needed for r^{2}SCAN and the three deorbitalized versions considered in the preceding plot. One sees clearly how the SCF process for original r^{2}SCAN converges in consistently fewer cycles than for any of the three deorbitalized variants. The RPP-type deorbitalizers perform quite reasonably but with a number of outliers. In contrast PC_{opt} has a rather larger number of outliers which cancel its edge in the time-per-cycles metric. Note also the scatter plot of SCF cycles needed versus the r^{2}SCAN requirement in Fig. 6. The smoothed r^{2}SCAN-L(SRPP) does provide consistent improvement upon the performance of r^{2}SCAN-L(RPP), with a few exceptions among the semiconductors and simple metals.

In sum, while there will be remaining issues in achieving self-consistency with Laplacian-dependent functionals, it is clear that such issues are ameliorated significantly by having a smoother potential.

D. Detailed analysis of computational parameter dependence

Given the importance of materials calculations with plane-wave basis codes such as VASP and the significant performance differences between molecules and solids for such codes, investigation of computational technique and parameter choice effects is imperative. We pursue that in two ways. In this subsection we examine the dependence of timing results on various run parameter choices. In the following subsection we consider the equation of state (cold curve) of Al and a short AIMD calculation for it.

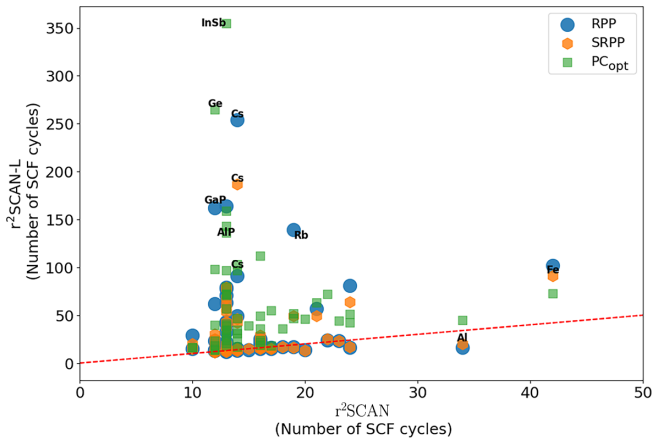

FIG. 6. Scatter plot showing the number of SCF cycles for 55 solids calculated using the deorbitalized functionals relative to the number of cycles required with the r^{2}SCAN functional. The red dotted line is the locus of values for the deorbitalized functionals that are equal to the r^{2}SCAN values.

Table VIII provides timing information for r^{2}SCAN versus r^{2}SCAN-L deorbitalized via RPP and SRPP for the 55 solid test set. It shows the effects of differing choices of the energy cutoff, convergence parameter, and minimization algorithm. Cases labeled "0" through "3" successively reduce the convergence tolerances while keeping the SCF minimization procedure fixed as the preconditioned conjugate gradient method. That is the recommended option for meta-GGA exchange-correlation functionals. Cases 4, 5, and 6 explore effects of the use of less expensive diagonalization algorithms.

Note that for all cases there is a significant advantage for the deorbitalized forms with respect to the parent functional for the time taken by a single calculation of electronic orbitals. The speed-up stays a little over a factor of 2, maybe better for the fastest eigensolver.

In contrast, the advantage in terms of the number of cycles needed to reach self-consistency for the gKS procedure used with r^{2}SCAN over the deorbitalized forms and their pure KS potential does vary quite a bit depending on the tightness of convergence criteria. gKS loses its advantage relative to deorbitalized KS as convergence is loosened and SRPP loses its advantage relative to RPP. Ultimately, for Case 3, the sloppiest one for preconditioned conjugate gradients and Case 6, the sloppiest overall, there is basically no difference in performance among the three strategies in this regard. Therefore the total time speed-up of deorbitalization is quite dramatic, almost a factor of 2. (It may seem peculiar that all functionals in Case 6 take substantially more cycles to achieve self-consistency than Case 3, with both larger plane-wave cutoff and stricter convergence tolerance. This is a result of the instability of the RMM-DIIS, which makes sacrifices in stability to achieve faster overall times [57]).

There is a plausible, simple explanation for such a finding. Reducing the cutoff energy amounts to introducing a low-pass filter that eliminates a good deal of noise in the potential. Though the r^{2}SCAN-L(RPP) and (SRPP) potentials have very different noise characteristics, it is reasonable to suppose that those differences are substantially removed by smoothing with a low-energy cutoff. Similarly, a less demanding tolerance means greater acceptance of effects of noise in the potential, reducing their consequences. We hypothesize that the smooth atomic-like basis used in molecular calculations is coarse relative to individual plane waves, therefore causing

TABLE VIII. Parameter and SCF algorithm dependence of timing for computing the set of 55 solids, for r^{2}SCAN itself, and r^{2}SCAN-L deorbitalized with RPP or SRPP. E_{cut} is the plane-wave cutoff energy; E_{diff} is the energy tolerance used to end the self-consistency cycle. The algorithms to solve the KS or gKS equation, using the keyword terminology for the ALGO input parameter in VASP, are (All) preconditioned conjugate gradient, (Normal) blocked Davidson iteration, (Fast) hybrid of block-Davidson and RMM-DIIS (Residual Minimization Method with Direct Inversion in the Iterative Subspace), and (Very Fast) RMM-DIIS.

	Case 0	Case 1	Case 2	Case 3	Case 4	Case 5	Case 6
Algorithm	All	All	All	All	Normal	Fast	Very Fast
E_{diff} (eV)	1×10^{-6}	2.72×10^{-5}	1×10^{-6}	2.72×10^{-5}	1×10^{-6}	1×10^{-6}	1×10^{-4}
E_{cut} (eV)	800	800	600	600	800	800	500
Average time							
r^{2}SCAN	110.05	101.28	95.51	81.47	112.26	104.26	58.37
RPP	109.54	63.78	55.23	42.02	103.97	63.11	22.66
SRPP	88.95	59.11	55.56	45.56	111.93	79.25	23.62
Average SCF cycles							
r^{2}SCAN	15.64	12.67	15.78	12.78	12.91	12.93	17.36
RPP	40.35	20.93	20.11	13.75	29.96	27.33	18.51
SRPP	30.49	17.55	17.49	13.69	29.09	30.80	18.75
Average time/cycle							
r^{2}SCAN	6.93	7.74	5.96	6.16	8.59	7.91	3.34
RPP	2.91	3.14	2.77	2.98	3.73	2.45	1.21
SRPP	2.97	3.32	3.03	3.21	4.11	2.83	1.24

a similar noise reduction in the potential and yielding the "egalitarian" timing results seen for these calculations.

E. Molecular dynamics of aluminum

For context, in Table IX we provide the timing and SCF count for calculating the static lattice fcc Al equation of state at zero temperature. The data are averages over runs at 12 lattice parameters, 3.8484 Å $\leqslant a_0 \leqslant$ 4.1146 Å. (At each lattice constant, the calculation was started from the same density, not from the equilibrium density of the preceding lattice constant. This technical aspect is of importance later.)

Solid Al is a particularly advantageous case for deorbitalization. Consistent with the discussion above about the 55 solid test set (recall Table VII), all three deorbitalizations (PC$_{opt}$, RPP, SRPP) are substantially faster in total time than the parent functional. The spreads are even better for r^{2}SCAN-L(RPP) and (PC$_{opt}$), and as good as the parent for (SRPP). Also as expected, the RPP- and SRPP-deorbitalized functionals outperform PC$_{opt}$ substantially with regard to the required number of SCF cycles.

TABLE IX. Timings (in seconds, s) and number of SCF cycles required for computing the zero-temperature fcc Al static lattice equation of state for r^{2}SCAN and three deorbitalizations, with PBE values for context.

		r^{2}SCAN-L			
fcc Al	r^{2}SCAN	PC$_{opt}$	RPP	SRPP	PBE
Total time	990.89	611.87	366.93	415.89	296.04
Average time	82.57	50.99	30.58	34.66	24.67
Avg. nr. SCF cycles	26.75	45.00	17.58	20.83	12.42
Spread	23.00	51.00	9.00	19.00	4.00
Avg. time per cycle	3.12	1.16	1.75	1.68	2.00
Spread	0.42	0.32	0.21	0.41	0.30

Those rather encouraging timing and cycle count results would lead to the expectation that the SRPP and RPP functionals would outperform the parent in driving AIMD. To investigate that, we obtained timing statistics for a short AIMD simulation of liquid-phase aluminum.

The simulation system consisted of 108 atoms, at bulk density $\rho = 2.34$ g/cm^3 in a 12.7239 × 12.7239 × 12.7239 Å^3 cell. The Γ-point was used to sample the Brillouin zone. In VASP 5.4.4, the system was treated with a three-electron PAW effective potential ($3s^2\ 3p^1$ valence, 10 electrons in the core; denoted PAW_PBE Al_GW). Nonspherical contributions within the PAW spheres were included self-consistently. Minimization used the RMM-DIIS algorithm with energy cutoff set to 500 eV, as in Case 6 in Table VIII. The self-consistent energy convergence tolerance E_{diff} was 1×10^{-4} eV. Approximate Fermi-type thermal smearing with a width of 0.088 155 5 eV was applied, and the initial temperature set to 1023 K. The molecular dynamics was done in the canonical (*NVT*) ensemble using the Verlet algorithm and a Nosé thermostat. 6501 steps with time-step 0.941 femtoseconds were taken for each simulation. Each calculation utilized 5 nodes on the University of Florida HiperGator cluster (Gen. 3), with 64 cores per node (total of 320 cores) and 4 GB of memory per core (1280 GB total).

Figure 7 gives the resulting timing statistics. Total times in hours are in the upper panel, Fig. 7(a), along with the total number of SCF cycles. The time per SCF cycle is shown in the lower panel Fig. 7(b). The outcome is that all of the deorbitalized functionals are at a disadvantage with respect to the parent functional r^{2}SCAN for total run time. This is in contrast to what one would have expected from the fcc Al equation of state results just discussed.

Clearly, the problem is not in the time per SCF cycle. As with the Al equation of state, the best performers on a per-

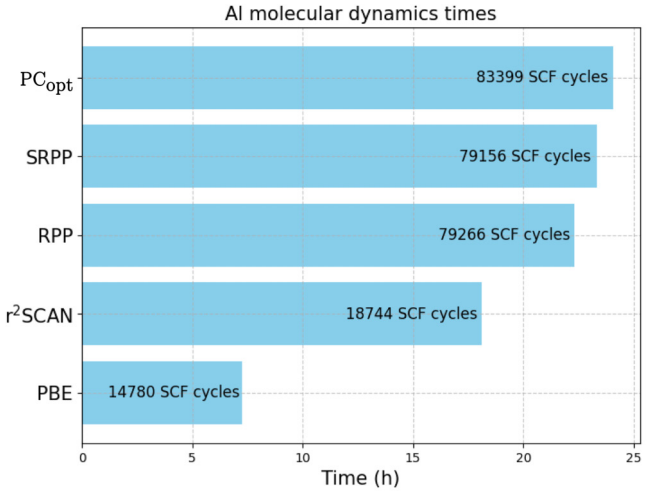

(a)

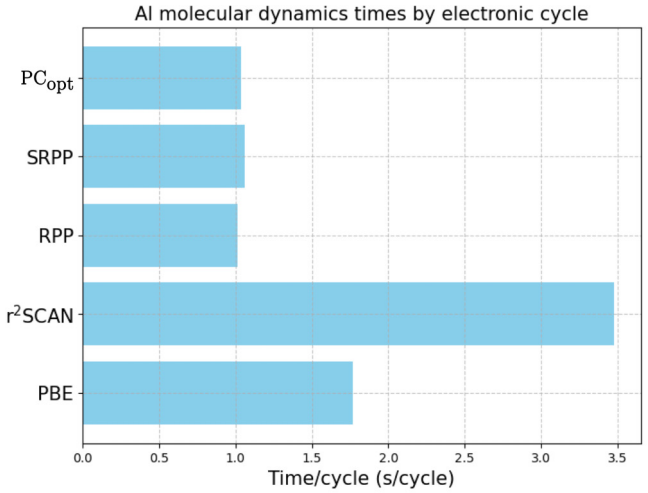

(b)

FIG. 7. Timing statistics for 6501 step AIMD simulation of liquid Al, using PBE, r^{2}SCAN, and r^{2}SCAN-L with several deorbitalization strategies. (a) Bar chart showing total run times in hours; total number of SCF cycles taken also noted. (b) Time per electronic cycle, in seconds.

cycle basis are the deorbitalized functionals, particularly RPP and SRPP. They out-perform even PBE. But for the AIMD, the number of SCF cycles needed for those deorbitalized functionals is almost prohibitively high, over four times the number needed for the parent functional, and over five times that needed for PBE.

This excessive SCF cycle count also is in marked contradiction to our findings for the 55 solids. Recall Table VIII. It shows that for the lowest accuracy tolerances in cutoff energy and SCF convergence (Case 6), the same as employed in the AIMD, the number of cycles needed for the deorbitalized functionals and the parent functional are roughly the same. That clearly is not the case in the AIMD driven by any of the deorbitalizers.

One way to characterize this problematic cycle count is that convergence to self-consistency from the fully converged density of the previous MD step is not that much quicker than convergence from an LCAO density (12 cycles average per MD step for SRPP, in contrast to 14 cycles average over the test set and 18 to 21 for the equation of state calculation for Al). The behavior also is in contrast with the dramatic reduction of PBE and r^{2}SCAN requirements to fewer than 3 cycles average per step. This may be an unpleasant consequence of the inclusion of the density Laplacian in the X functional and associated sensitivity to seemingly small changes in the density. A peculiarity is that a tolerance of $E_{\rm diff} = 2.75 \times 10^{-5}$ needs an average of 14 cycles to converge in the case of the 55 element test set (see Table VIII) while, on the other hand, use of $E_{\rm diff} = 1 \times 10^{-4}$ in the MD needs 18 cycles. The difficulty is that though RMM-DIIS is extremely fast it is less stable than the other solvers.

We have pursued two diagnostic follow-ups which indicate that the issue is quite complex and not readily resolvable. First, altering the MD timestep should provide a quick consistency check regarding the behavior. We find remarkably that the convergence issues, if anything, *increase* as the timestep is decreased. See Table X. Since this obviously cannot be the case in the limit of zero time step, something peculiar is happening but we have been unable to identify the cause.

Secondly, investigation of the number of SCF cycles needed as a function of simulation time shows a rather intriguing trend. The RPP and SRPP deorbitalized functionals start out with convergence times that are quite competitive to r^{2}SCAN and PBE. Only gradually, over about 10 MD steps, do they settle down to the more slowly converging behavior. The slowdown in convergence is correlated to increased fluctuations in convergence performance, symptomatic of an unresolved stability issue. This behavior is documented in Fig. 8. Perhaps it is noteworthy that, of the three deorbitalizers, the one with smoothest potential, SRPP, has the smallest fluctuations in cycles-per-step. We have sought diagnostic insight from calculating mean-square displacements and radial distribution functions for both $T = 1093$ and 298 K AIMD but without much gain in understanding. Plots of the results are in the Supplemental Material [40].

The behavior suggests that tendencies to instability in the deorbitalized forms take some SCF cycles to show up and might be ameliorated by taking an occasional step using, e.g., PBE, to find the density. We tried one such strategy. At each MD step, the first five SCF cycles were done with PBE, then continued with the selected deorbitalized functional. Unfortunately, this strategy actually increased the number of SCF cycles instead of reducing them.

We also analyzed the Hellmann-Feynman forces during the course of this simulation. The detailed analysis is provided in Fig. 4 of the Supplemental Material [40], which shows the maximum, minimum, and median forces in the z direction for the first 50 and 500 MD steps. No outliers are observed, and the median values remain close to zero for all functionals tested. That indicates a symmetric distribution of forces around zero, without systematic bias introduced by the deorbitalized functionals.

V. DISCUSSION AND CONCLUDING REMARKS

Deorbitalizing a conventional meta-GGA XC functional is motivated by two closely related goals. The first is to

TABLE X. Total times for the molecular dynamics of Al using the SRPP deorbitalizer for different values of time step.

XC functional	Time step (POTIM)	Total time (s)	Number of SCF cycles	Time by cycle (s)	Average temperature (K)
r^{2}SCAN-L(SRPP)	1.4	87897.82	78872	1.11	1023.021
	0.940793	83935.23	79156	1.06	1022.869
	0.5	95314.36	86477	1.10	1022.973
r^{2}SCAN-L(RPP)	0.940793	80395.09	79266	1.01	1022.995
	0.5	86879.67	87786	0.99	1023.052
r^{2}SCAN	0.940793	65212.99	18744	3.48	1023.058
	0.5	54600.70	13554	4.03	1023.056

regain the interpretability provided by the locality of the KS potential. The second is to achieve major computational speedups as a consequence of that simplification without compromise of predictive accuracy. Thus, the simultaneous focus of this paper is on issues of both functional accuracy and speed. In that regard, Laplacian-dependent deorbitalizers are two-edged swords. While providing useful deorbitalization accuracy, they can introduce highly spiky functions that can be impediments to computational speed.

We have addressed those competing effects by introducing a smoothness measure, I^{deorb}, for an XC potential to motivate the use of deorbitalizers (SRPP and SRPP2) designed with smoothness in mind. Both preserve fundamental constraints respected by the recent OFR2 deorbitalization of r^{2}SCAN and do not degrade norm satisfaction significantly. The result is improvement for both accuracy and timing objectives. Our timing study concentrates on approaches (Gaussian basis sets, plane waves, and PAW pseudopotentials) used in AIMD and high through-put calculations, and should provide ballpark expectations for any such code. Tuning or adapting these codes for optimal performance for Laplacian-based functionals, especially for AIMD, would be a welcome next step to achieve the full promise of deorbitalization.

We have used the smoothness measure, I^{deorb}, to probe for and control instability sources in the XC potential of deorbitalized meta-GGAs. In consequence, SRPP and SRPP2 produce noticeably smoother kinetic and exchange potentials than other deorbitalizers. Notably, for these smoothed variants of RPP, the constraint compliance for slowly varying densities imposed by the RPP comes with a much smaller penalty in predictive performance for highly inhomogeneous systems than one might expect from the behavior of the RPP. The smoothed functionals improve upon RPP markedly for the G3 molecular test set, though the deorbitalized form still is not competitive with r^{2}SCAN-L(PC$_{\text{opt}}$) for heats of formation. The (SRPP2) variant, though less effective than (SRPP) on the molecular cases, is equal or better on the solids and delivers better timing performance. It is plausible that this gain is a consequence of the r^{2}SCAN-L(SRPP2) X potential being smoother than the SRPP-deorbitalized one. It also is plausible that smoothing along the lines we have presented would be helpful in reaching desired performance goals for deorbitalized finite-temperature functionals [58,59].

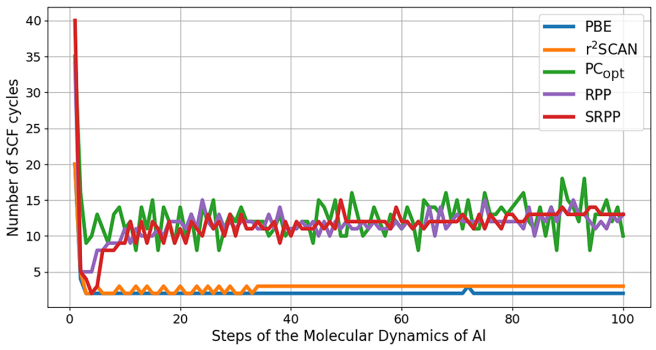

FIG. 8. Number of SCF cycles to convergence per molecular dynamics step for different approximations, plotted for the first 100 MD time steps.

The implications for timing performance are complicated and unfortunately somewhat obscure. For molecules, both the time per SCF cycle and the number of cycles needed to reach convergence are essentially the same for both the parent and deorbitalized functionals. For fixed (static) solid geometries, however, these particular deorbitalized meta-GGAs significantly outperform the explicitly orbital dependent meta-GGA parent (used in gKS form) so far as time per SCF cycle is concerned. While the deorbitalized forms [r^{2}SCAN-L(SRPP) or (SRPP2)] need more cycles to reach self-consistent convergence, the increment is not so large as to offset the much shorter cycle time. As a result, these are much faster than r^{2}SCAN for static lattice solid calculations, as seen in Tables VII, VIII, and IX.

That advantage does not propagate into the one AIMD example we have tried. It appears that the density Laplacian dependence in the deorbitalized functionals introduces instabilities that greatly increase the number of SCF cycles needed in the AIMD context. It might seem that the XC potential would be sensitive to small perturbations in the density because of the Laplacian, so that potentials for successive AIMD steps would be different enough to lead to unusual variation in the density, and thus slower SCF convergence. However, our limited testing with reduced AIMD step-time is inconsistent with this argument. Similarly, there is no obvious clue as to the cause of the problematic behavior in the average SCF cycle time versus its spread. Recall that Table VII shows that r^{2}SCAN deorbitalized by SRPP, SRPP2, and RPP all have similar ratios of spread of time per cycle to average time per cycle, and the ratio for SRPP (2.35) is slightly below that for RPP (2.51).

Because Gaussian basis functions are themselves smooth and are equivalent to fixed combinations of many plane waves, molecules calculated with Gaussian basis sets behave, oddly

enough, like the cruder and faster plane-wave calculations, in the sense that there is little distinction in timing among deorbitalizer forms. Utilization of a smooth, analytical basis apparently has a stabilizing effect that is a counterpart to reduction of the energy cutoff in a plane-wave code.

Our limited AIMD calculations also display a third, somewhat discomfiting behavior. As for the case of lower accuracy calculations for the equation of state, deorbitalized functions outperform the orbital-dependent parent on a per-cycle basis, while smoothed and unsmoothed deorbitalizers have similar SCF convergence rates. But PBE and r^{2}SCAN perform the task specific to MD, namely finding orbitals for a new set of nuclear positions starting from the density for a modestly different set of positions, in two or three SCF cycles. In contrast, the deorbitalized forms used here take almost the same number of cycles in starting from the previous converged density for the previous AIMD step as they do when starting from, say, an LCAO density. An attempt to start at each step with a PBE density did not help. The causes are undiagnosed.

Finally, it may be advantageous to use the measure of noise we defined as an aid to construction of deorbitalizers with yet smoother potentials, either by optimizing the switching function between iso-orbital and slowly varying limits or strategically modifying "appropriate norms" in the deorbitalizer or parent functional. This is the focus of ongoing research.

ACKNOWLEDGMENTS

We thank Valentin V. Karasiev for assistance regarding AIMD calculations with VASP. Work supported by U.S. National Science Foundation Grant No. DMR-1912618.

DATA AVAILABILITY

The data that support the findings of this article are openly available [60].

[1] J. P. Perdew and K. Schmidt, Jacob's ladder of density functional approximations for the exchange-correlation energy, AIP Conf. Proc. **577**, 1 (2001).

[2] A. M. Teale, T. Helgaker, A. Savin, C. Adamo, B. Aradi, A. V. Arbuznikov, P. W. Ayers, E. J. Baerends, V. Barone, P. Calaminici, E. Cancès, E. A. Carter, P. K. Chattaraj, H. Chermette, I. Ciofini, T. D. Crawford, F. De Proft, J. F. Dobson, C. Draxl, T. Frauenheim, *et al.*, DFT exchange: Sharing perspectives on the workhorse of quantum chemistry and materials science, Phys. Chem. Chem. Phys. **24**, 28700 (2022).

[3] J. Sun, A. Ruzsinszky, and J. P. Perdew, Strongly constrained and appropriately normed semilocal density functional, Phys. Rev. Lett. **115**, 036402 (2015).

[4] J. Sun, R. C. Remsing, Y. Zhang, Z. Sun, A. Ruzsinszky, H. Peng, Z. Yang, A. Paul, U. Waghmare, X. Wu, M. L. Klein, and J. P. Perdew, Accurate first-principles structures and energies of diversely bonded systems from an efficient density functional, Nat. Chem. **8**, 831 (2016).

[5] J. W. Furness and J. Sun, Enhancing the efficiency of density functionals with an improved iso-orbital indicator, Phys. Rev. B **99**, 041119(R) (2019).

[6] A. P. Bartók and J. R. Yates, Regularized SCAN functional, J. Chem. Phys. **150**, 161101 (2019).

[7] J. W. Furness, A. D. Kaplan, J. Ning, J. P. Perdew, and J. Sun, Accurate and numerically efficient r^{2}SCAN meta-generalized gradient approximation, J. Phys. Chem. Lett. **11**, 8208 (2020).

[8] G.-X. Zhang, A. M. Reilly, A. Tkatchenko, and M. Scheffler, Performance of various density-functional approximations for cohesive properties of 64 bulk solids, New J. Phys. **20**, 063020 (2018).

[9] P. Kovács, F. Tran, P. Blaha, and G. K. H. Madsen, Comparative study of the PBE and SCAN functionals: The particular case of alkali metals, J. Chem. Phys. **150**, 164119 (2019).

[10] D. Mejía-Rodríguez and S. B. Trickey, Analysis of overmagnetization of elemental transition metal solids from the SCAN density functional, Phys. Rev. B **100**, 041113(R) (2019).

[11] A. D. Becke and K. E. Edgecombe, A simple measure of electron localization in atomic and molecular systems, J. Chem. Phys. **92**, 5397 (1990).

[12] J. Sun, B. Xiao, Y. Fang, R. Haunschild, P. Hao, A. Ruzsinszky, G. I. Csonka, G. E. Scuseria, and J. P. Perdew, Density functionals that recognize covalent, metallic, and weak bonds, Phys. Rev. Lett. **111**, 106401 (2013).

[13] D. Mejia-Rodriguez and S. B. Trickey, Deorbitalization strategies for meta-generalized-gradient-approximation exchange-correlation functionals, Phys. Rev. A **96**, 052512 (2017).

[14] N. A. W. Holzwarth, M. Torrent, J.-B. Charraud, and M. Côté, Cubic spline solver for generalized density functional treatments of atoms and generation of atomic datasets for use with exchange-correlation functionals including meta-GGA, Phys. Rev. B **105**, 125144 (2022).

[15] Y. Yao and Y. Kanai, Plane-wave pseudopotential implementation and performance of SCAN meta-GGA exchange-correlation functional for extended systems, J. Chem. Phys. **146**, 224105 (2017).

[16] S. Lehtola and M. A. L. Marques, Many recent density functionals are numerically ill-behaved, J. Chem. Phys. **157**, 174114 (2022).

[17] P. Bonfà, S. Sharma, and J. Dewhurst, Partially deorbitalized meta-GGA, Comput. Mater. Today **1**, 100002 (2024).

[18] D. Mejia-Rodriguez and S. B. Trickey, Deorbitalized meta-GGA exchange-correlation functionals in solids, Phys. Rev. B **98**, 115161 (2018).

[19] D. Mejía-Rodríguez and S. B. Trickey, Meta-GGA performance in solids at almost GGA cost, Phys. Rev. B **102**, 121109(R) (2020).

[20] W. Mi, K. Luo, S. B. Trickey, and M. Pavanello, Orbital-free density functional theory: An attractive electronic structure method for large-scale first-principles simulations, Chem. Rev. **123**, 12039 (2023).

[21] J. P. Perdew and L. A. Constantin, Laplacian-level density functionals for the kinetic energy density and exchange-correlation energy, Phys. Rev. B **75**, 155109 (2007).

[22] A. C. Cancio, D. Stewart, and A. Kuna, Visualization and analysis of the Kohn-Sham kinetic energy density and its orbital-free description in molecules, J. Chem. Phys. **144**, 084107 (2016).

[23] D. Rani, S. Jana, M. K. Niranjan, and P. Samal, First-principle investigation of structural, electronic, and phase stabilities in chalcopyrite semiconductors: Insights from Meta-GGA functionals, J. Phys.: Condens. Matter **36**, 165502 (2024).

[24] Y. Zhang, Advancing DFT predictions in Cu-chalcogenides with full-yet-shallow 3*d*-orbitals: Meta-GGA plus Hubbard-like U correction, J. Chem. Phys. **161**, 174109 (2024).

[25] A. C. Cancio and J. J. Redd, Visualisation and orbital-free parametrisation of the large-Z scaling of the kinetic energy density of atoms, Mol. Phys. **115**, 618 (2017).

[26] H. Francisco, A. C. Cancio, and S. B. Trickey, Removing orbital-dependence to improve exchange-correlation functional accuracy, J. Phys. Chem. A **129**, 10240 (2025).

[27] A. D. Kaplan and J. P. Perdew, Laplacian-level meta-generalized gradient approximation for solid and liquid metals, Phys. Rev. Mater. **6**, 083803 (2022).

[28] H. Francisco, A. C. Cancio, and S. B. Trickey, Reworking the Tao-Mo exchange–correlation functional. III. Improved deorbitalization strategy and faithful deorbitalization, J. Phys. Chem. A **128**, 6010 (2024).

[29] J. Tao and Y. Mo, Accurate semilocal density functional for condensed-matter physics and quantum chemistry, Phys. Rev. Lett. **117**, 073001 (2016).

[30] P. de Silva and C. Corminboeuf, Simultaneous visualization of covalent and noncovalent interactions using regions of density overlap, J. Chem. Theor. Comput. **10**, 3745 (2014).

[31] P. de Silva and C. Corminboeuf, Local hybrid functionals with orbital-free mixing functions and balanced elimination of self-interaction error, J. Chem. Phys. **142**, 074112 (2015).

[32] P. de Silva and C. Corminboeuf, Communication: A new class of non-empirical explicit density functionals on the third rung of Jacob's ladder, J. Chem. Phys. **143**, 111105 (2015).

[33] G. Kresse and J. Furthmüller, Efficient iterative schemes for *ab initio* total-energy calculations using a plane-wave basis set, Phys. Rev. B **54**, 11169 (1996).

[34] G. Kresse and D. Joubert, From ultrasoft pseudopotentials to the projector augmented-wave method, Phys. Rev. B **59**, 1758 (1999).

[35] D. A. Kirzhnits, Quantum corrections to the Thomas–Fermi equation, J. Exptl. Theo. Phys. (U.S.S.R.) **32**, 115 (1957) [Sov. Phys. JETP **5**, 64 (1957)].

[36] C. H. Hodges, Quantum corrections to the thomas–Fermi approximation—the Kirzhnits method, Can. J. Phys. **51**, 1428 (1973).

[37] M. Levy and H. Ou-Yang, Exact properties of the Pauli potential for the square root of the electron density and the kinetic energy functional, Phys. Rev. A **38**, 625 (1988).

[38] D. Mejía-Rodriguez, densities (version 0.1), Available from author upon request under GNU General Public License, v3. (2023).

[39] T. Koga, K. Kanayama, S. Watanabe, and A. J. Thakkar, Analytical Hartree-Fock wave functions subject to cusp and asymptotic constraints: He to Xe, Li^+ to Cs^+, H to I, Int. J. Quantum Chem. **71**, 491 (1999).

[40] See Supplemental Material at http://link.aps.org/supplemental/10.1103/rbf1-cp89 for a detailed, system-by-system tabulation of the numerical results of the test calculations against standard molecular and solid test sets, as well as system-by-system SCF timing and SCF cycle count tabulations, corresponding to the plot of SCF cycle count for each of the first 100 AIMD steps in Fig. 8. In addition, we provide plots of mean-squared displacements and radial distribution functions of Al from the various XC functionals driving AIMD at $T = 298$ and 1023 K.

[41] R. van Leeuwen and E. J. Baerends, Exchange-correlation potential with correct asymptotic behavior, Phys. Rev. A **49**, 2421 (1994).

[42] A. C. Cancio, C. E. Wagner, and S. A. Wood, Laplacian-based models for the exchange energy, Int. J. Quantum Chem. **112**, 3796 (2012).

[43] E. Aprà, E. J. Bylaska, W. A. de Jong, N. Govind, K. Kowalski, T. P. Straatsma, M. Valiev, H. J. J. van Dam, Y. Alexeev, J. Anchell, V. Anisimov, F. W. Aquino, R. Atta-Fynn, J. Autschbach, N. P. Bauman, J. C. Becca, D. E. Bernholdt, K. Bhaskaran-Nair, S. Bogatko, P. Borowski, *et al.*, NWChem: Past, present, and future, J. Chem. Phys. **152**, 184102 (2020).

[44] L. A. Curtiss, K. Raghavachari, P. C. Redfern, and J. A. Pople, Assessment of Gaussian-2 and density functional theories for the computation of enthalpies of formation, J. Chem. Phys. **106**, 1063 (1997).

[45] L. A. Curtiss, P. C. Redfern, K. Raghavachari, and J. A. Pople, Gaussian-3X (G3X) theory: Use of improved geometries, zero-point energies, and Hartree–Fock basis sets, J. Chem. Phys. **114**, 108 (2001).

[46] V. N. Staroverov, G. E. Scuseria, J. Tao, and J. P. Perdew, Comparative assessment of a new nonempirical density functional: Molecules and hydrogen-bonded complexes, J. Chem. Phys. **119**, 12129 (2003).

[47] V. N. Staroverov, G. E. Scuseria, J. Tao, and J. P. Perdew, Erratum: "Comparative assessment of a new nonempirical density functional: Molecules and hydrogen-bonded complexes" [J. Chem. Phys. **119**, 12129 (2003)], J. Chem. Phys. **121**, 11507 (2004).

[48] H. Francisco, A. C. Cancio, and S. B. Trickey, Reworking the Tao–Mo exchange-correlation functional. I. Reconsideration and simplification, J. Chem. Phys. **159**, 214102 (2023).

[49] H. Peng, Z.-H. Yang, J. P. Perdew, and J. Sun, Versatile van der Waals density functional based on a meta-generalized gradient approximation, Phys. Rev. X **6**, 041005 (2016).

[50] F. Tran, J. Stelzl, and P. Blaha, Rungs 1 to 4 of DFT Jacob's ladder: Extensive test on the lattice constant, bulk modulus, and cohesive energy of solids, J. Chem. Phys. **144**, 204120 (2016).

[51] F. Tran and P. Blaha, Importance of the kinetic energy density for band gap calculations in solids with density functional theory, J. Phys. Chem. A **121**, 3318 (2017).

[52] A. B. Alchagirov, J. P. Perdew, J. C. Boettger, R. C. Albers, and C. Fiolhais, Energy and pressure versus volume: Equations of state motivated by the stabilized jellium model, Phys. Rev. B **63**, 224115 (2001).

[53] S. J. Chakravorty, S. R. Gwaltney, E. R. Davidson, F. A. Parpia, and C. F. Fischer, Ground-state correlation energies for atomic ions with 3 to 18 electrons, Phys. Rev. A **47**, 3649 (1993).

[54] E. Engel and R. M. Dreizler, From explicit to implicit density functionals, J. Comput. Chem. **20**, 31 (1999).

[55] K. Burke, A. Cancio, T. Gould, and S. Pittalis, Locality of correlation in density functional theory, J. Chem. Phys. **145**, 054112 (2016).

[56] J. P. Perdew, K. Burke, and M. Ernzerhof, Generalized gradient approximation made simple, Phys. Rev. Lett. **77**, 3865 (1996); **78**, 1396(E) (1997).

[57] G. Kresse (2025), https://www.vasp.at/vasp-workshop/optelectron.pdf.

[58] V. V. Karasiev, D. I. Mihaylov, and S. X. Hu, Meta-GGA exchange-correlation free energy density functional to increase the accuracy of warm dense matter simulations, Phys. Rev. B **105**, L081109 (2022).

[59] V. Karasiev, K. Hilleke, and S. B. Trickey, Free-energy orbital-free density functional theory: Recent developments, perspective, and outlook, Electron. Struct. **7**, 013001 (2025).

[60] H. Francisco, B. Thapa, S. B. Trickey, and A. Cancio, Performance improvement of deorbitalized exchange-correlation functionals, Materials Cloud Archive (2025), https://archive.materialscloud.org/record/2025.141.